Article

Development and Phantom Validation of a Small-Form-Factor SWIR Emitter Probe for Hydration-Sensitive Spatial-Ratio Measurements in Gelatin-Intralipid Phantoms

Georgei Farouq * , Devang Vyas , Amir Zavareh

Posted Date: 5 March 2026

doi: 10.20944/preprints202603.0476.v1

Keywords: short-wave infrared spectroscopy (swirs); hydration sensing; gelatin–intralipid phantom; diffuse reflectance; spatially resolved spectroscopy; Monte Carlo lookup tables; small-form-factor sensor

doi:10.20944/preprints202603.0476.v1

Article

Development and Phantom Validation of a Small-Form-Factor SWIR Emitter Probe for Hydration-Sensitive Spatial-Ratio Measurements in Gelatin-Intralipid Phantoms

Georgei Farouq [1], Devang Vyas [2] and Amir Tofghi Zavareh [3]

[1] Department of Engineering Technology and Industrial Distribution, Texas A&M University, College Station, TX 77843, USA
[2] Department of Biomedical Engineering, Texas A&M University, College Station, TX 77843, USA
[3] Department of Engineering Technology and Industrial Distribution, Department of Biomedical Engineering, Center for Remote Health Technologies and Systems, Texas A&M University, College Station, TX 77843, USA
* Correspondence: amirtofighi@tamu.edu

Abstract

Non-invasive assessment of tissue water content is clinically relevant for edema detection, fluid management, and monitoring of local inflammation. In the short-wave infrared (SWIR), water exhibits strong absorption near 1450 nm with a secondary band near 1650 nm, enabling hydration-sensitive reflectance measurements. However, many SWIR systems rely on spectrometers or high-power broadband sources, limiting translation to compact or wearable platforms. We present a compact SWIR diffuse-reflectance probe built from small-form-factor components using four discrete LEDs (1450 nm and 1650 nm) and a single photodetector to acquire spatially resolved measurements at two source–detector separations (4.5 mm and 7 mm). Probe-geometry-matched Monte Carlo simulations were used to generate lookup tables relating reduced scattering to same-wavelength spatial ratios. A diffusion-based forward model was then used to perform a calibration-anchored water-fraction consistency analysis. Eight gelatin–Intralipid phantoms spanning two scattering conditions and formulation-defined water fractions were evaluated. Spatial-ratio signatures were repeatable and monotonic with nominal water fraction, yielding a mean absolute percent error of 1.55% and a maximum absolute percent error of 3.33% under absorption-consistent conditions. These results demonstrate the feasibility of compact SWIR ratio sensing for controlled hydration changes in tissue-mimicking phantoms and provide a modeling framework for future extension to unknown or in vivo samples.

Keywords: short-wave infrared spectroscopy (swirs); hydration sensing; gelatin–intralipid phantom; diffuse reflectance; spatially resolved spectroscopy; Monte Carlo lookup tables; small-form-factor sensor

---

1. Introduction

Non-invasive assessment of tissue water content is clinically relevant for edema evaluation, fluid-management guidance, and monitoring of local inflammation [1]. Conventional bedside assessments (e.g., pitting and skin turgor) are subjective and operator dependent [2,3]. Optical methods in the near-infrared (NIR) and short-wave infrared (SWIR) are attractive because tissue attenuation in these bands is strongly influenced by water absorption while remaining compatible with small-form-factor optoelectronics [4,5].

In the SWIR, water exhibits a strong O–H combination band near 1450 nm and a weaker band near 1650 nm [5–7]. Above approximately 1300 nm, absorption from dominant visible/NIR chromophores (e.g., hemoglobin and melanin) is reduced, and water can become a principal contributor to attenuation in soft tissue [5,8–10]. Diffuse reflectance at water-sensitive wavelengths therefore decreases with increasing bulk water content [2,9]. The present work uses 1450 nm for high hydration sensitivity and 1650 nm as a secondary band with lower absorption, providing a practical trade-off between sensitivity and sampling depth [4,8–10]. More strongly absorptive bands near 1950 nm offer limited penetration and impose substantial implementation constraints for compact reflectance sensing [4,5,8,10,11].

Many reported hydration-related NIR/SWIR systems rely on spectrometers, tunable sources, or multispectral imaging architectures that increase size, cost, and power consumption [2,4,8,9,12,13]. Discrete-wavelength reflectance sensing provides an alternative path to miniaturization by using compact emitters at selected water bands and a single photodetector [6,14–16].

To reduce sensitivity to subject- and coupling-dependent variability (e.g., scattering changes due to microstructure, contact pressure, and boundary effects), spatially resolved measurements at multiple source–detector separations (SDS) can be used [17–19]. Because absorption and reduced scattering affect the radial decay of diffuse reflectance differently, multi-SDS ratios provide additional constraints for interpreting hydration-sensitive changes compared with a single-distance measurement [17–21].

Here we develop and validate a compact SWIR reflectance probe that acquires two-wavelength, two-SDS measurements (1450/1650 nm; 4.5/7 mm) in controlled gelatin–Intralipid phantoms spanning recipe-defined water fractions and multiple scattering conditions [22–26]. Monte Carlo simulations matched to the probe geometry are used to generate lookup tables for interpreting spatial ratios [27–29]. In this prototype, detection is performed with an amplified laboratory InGaAs photodetector module [4,6,14].

The objective of this study is to validate that a compact SWIR probe using small-form-factor emitters produces repeatable, monotonic spatial-ratio signatures of hydration in controlled gelatin–Intralipid phantoms with recipe-defined water fraction [2,6,9,14,24]. Specifically, we evaluate (i) monotonic dependence of same-wavelength spatial ratios on nominal phantom water fraction under fixed acquisition conditions, and (ii) agreement of an absorption-assigned, probe-matched inversion pipeline with the recipe-defined value as a consistency check, rather than blind estimation of $\mu_a(\lambda)$ or f_w from reflectance alone [17,19,29].

This workflow is critical as it decouples instrument response from model-based inference, rigorously benchmarks hydration sensitivity against a ground-truth optical standard, and establishes a physically constrained calibration pathway that strengthens confidence in subsequent translation to heterogeneous biological tissue where $\mu_{a,\lambda}$ and scattering cannot be independently specified.

2. Materials and Methods

Materials and Methods describe: (i) gelatin–Intralipid phantom fabrication with recipe-defined (nominal) $f_{w,\mathrm{true}}$, (ii) probe-geometry-matched MC LUT generation used to invert μ_s' from spatial ratios conditional on assigned $\mu_a(\lambda)$, (iii) the benchtop measurement hardware and optical interface, and (iv) a ratio-based inversion used as a calibration-anchored consistency check rather than blind recovery for unknown samples [18,19,29].

2.1. Phantom Production Pipeline & Rationale

2.1.1. Motivation for In Vitro Phantom Use

Gelatin-based phantoms provide a controllable, repeatable test medium for early-stage probe validation prior to in vivo studies, where inter-subject variability (thickness, hydration, lipids, coupling, and scattering) complicates calibration and characterization [22,30,31]. In this work, phantoms were selected to enable systematic variation of bulk water fraction and scattering while maintaining a stable, contact-compatible surface [22,24].

2.1.2. Gelatin Hydrogel Matrix Rationale

Gelatin hydrogels are widely used tissue-mimicking phantoms because they form mechanically stable, water-rich matrices suitable for repeatable contact measurements [22,24,25,30]. Here gelatin is treated primarily as a mechanical scaffold; water is the dominant SWIR absorber over 1450–1650 nm. [5,9,10].

doi:10.20944/preprints202603.0476.v1

2.1.3. Use of Intralipid as a Scattering Agent

To emulate tissue-like multiple scattering, Intralipid is used as a standard lipid-emulsion scattering agent with well-characterized optical behavior [23,25,26,32]. Because Intralipid® is an emulsion of lipid droplets in a water background, its absorption is weak and, in practice, close to that of water; therefore, it is treated primarily as a scattering agent in the SWIR bands used here [33]. Phantoms were fabricated with 10% and 20% (w/w) Intralipid® 20% stock in the final mixture [23,26,32]. Unless otherwise stated, "10% Intralipid" denotes 10% w/w *Intralipid® 20% stock loading* in the final mixture (e.g., 1.50 g stock in a 15.0 g batch), and "20% Intralipid" denotes 20% w/w stock loading (e.g., 3.00 g stock in a 15.0 g batch) [23,32].

2.1.4. Gelatin Phantom Fabrication

Gelatin phantoms were fabricated by modifying the protocol of Jonasson et al. [24] with gravimetric mass preparation [22,30,31]. Two water-fraction quantities are distinguished: (i) the added-water fraction (added distilled water divided by total batch mass), and (ii) the true water fraction, which also accounts for solvent water in Intralipid® 20% stock (assumed 80% water by mass) [23,32]. The recipe-defined true water fraction is

$$f_{w,\text{true}} = \frac{m_{\text{water}} + 0.8\, m_{\text{IL}}}{m_{\text{total}}}, \tag{1}$$

where m denotes the mass of water intralipid and total gel, respectively. Gelatin's intrinsic absorption has been reported to closely track an aqueous background in the near-infrared; accordingly, at the strong SWIR water bands used here (1450 nm and 1650 nm) we neglect gelatin's intrinsic contribution relative to water and model $\mu_a(\lambda)$ as water-dominant [34]. Throughout, $f_{w,\text{true}}$ is treated as a nominal reference value (dominant uncertainties include Intralipid stock water-content assumption, handling/evaporation during heating, scale repeatability, and any non-homogeneity) [22,25,26].

Each phantom was prepared at a total batch mass of 15.0 g and cast to yield a flat, contact-stable surface [22,30]. Briefly, distilled water and gelatin were combined and allowed to bloom, then heated and stirred until homogeneous [22,25]. The solution was cooled to reduce emulsion stress, Intralipid® 20% stock was added and mixed, the mixture was vacuum-degassed, then poured into a mold and refrigerated overnight [22,31].

After fabrication, phantoms were sealed to minimize dehydration prior to measurement and were used only if visually homogeneous (no macroscopic creaming/stratification) [24–26]. Phantoms exhibiting visible phase separation were excluded from quantitative analysis because they violate the homogeneous-medium assumption used in both LUT generation and diffusion modeling [22,30]. Representative composition ranges and preparation photos are provided in the Supplementary Materials (Tables S1–S3 and Fig. S1); the specific formulations used in this study are listed in Table 1.

Table 1. Component masses used to prepare 15.0 g gelatin phantoms at two Intralipid® 20% stock loadings (10% and 20% of total batch mass). "Added-water (AW)" labels indicate the fraction of added distilled water by total batch mass. "True water content" accounts for water contained in Intralipid® 20% stock (assumed 80% water by mass): $f_{w,\text{true}} = (m_{\text{water}} + 0.8\, m_{\text{IL}})/m_{\text{total}}$.

Phantom	Intralipid stock loading (% of batch mass)	Water (g)	Gelatin (g)	Intralipid® 20% (g)	True water content (%)
70% AW	10%	10.50	3.000	1.50	78.00
73.68% AW	10%	11.052	2.448	1.50	81.68
75% AW	10%	11.25	2.250	1.50	83.00
80% AW	10%	12.00	1.500	1.50	88.00
62% AW	20%	9.300	2.700	3.00	78.00
65.68% AW	20%	9.852	2.148	3.00	81.68
67% AW	20%	10.050	1.950	3.00	83.00
72% AW	20%	10.800	1.200	3.00	88.00

2.2. *Monte Carlo Simulations for Probe-Specific LUT Generation*

Monte Carlo (MC) photon-transport simulations (MCmatlab) were used to generate probe-geometry-specific lookup tables (LUTs) that map the reduced scattering coefficient, μ_s', to expected diffuse-reflectance observables for the instrument's two source–detector separations (SDS) and collection constraints [27,28]. The purpose of the LUTs is to provide a probe-matched reference for how channel magnitudes and, critically, same-wavelength spatial ratios vary with μ_s' under specified absorption at each wavelength [19,21,28,29]. Key MC configuration parameters are summarized in the Supplementary Materials (Table S6).

2.2.1. Absorption Parameterization and Scope

Over 1450–1650 nm, absorption in gelatin–Intralipid hydrogels was modeled as water dominated (gelatin and lipid treated as secondary within a simplified model) [5,9,10,30,33,34]. Absorption was assigned as

$$\mu_a(\lambda) \approx f_w\, \mu_{a,\text{water}}(\lambda), \tag{2}$$

where $\mu_{a,\text{water}}(\lambda)$ was taken from the liquid-water dataset of Hale and Querry [5,7,8] and expressed in cm^{-1}. Within each wavelength sweep, $\mu_a(\lambda)$ was held fixed while μ_s' was varied; thus the LUT mapping ratio $\to \mu_s'$ is conditional on the assumed $\mu_a(\lambda)$ [18,19,29]. In this phantom validation study, the absorption coefficient, $\mu_a(\lambda)$, was prescribed based on the recipe-defined (nominal) water fraction, $f_{w,true}$, for each phantom formulation, thereby enabling evaluation of the inversion pipeline under absorption-consistent conditions. The present work is intentionally confined to controlled, optically defined phantoms to establish internal consistency and methodological validity. Extension of this framework to unknown or heterogeneous samples will necessitate a coupled absorption–scattering inversion strategy, in which $\mu_a(\lambda)$ and reduced scattering are jointly estimated from measured reflectance data. [29].

2.2.2. Simulation Geometry and Optical Properties

The phantom was modeled as a homogeneous rectangular slab with dimensions 3.5 cm × 3.5 cm × 1.2 cm, discretized on a 101 × 101 × 150 voxel grid to match fabricated gel dimensions [27]. To emulate the experimental optical head and suppress stray-photon collection, a thin optically black "super-absorbing" mask was placed directly above the gel surface, spanning the lateral extent of the domain, with a centered circular through-aperture of diameter 4 mm defining the collection aperture [18,29]. Photons intersecting the mask outside the aperture were terminated; photons passing through the aperture were allowed to propagate and be detected, so that the effective field-of-view and collection area were aperture limited, matching the experimental configuration.

The phantom was assigned wavelength-dependent $\mu_a(\lambda)$ and scattering $\mu_s(\lambda)$ with fixed anisotropy $g = 0.9$ [5]. To ensure that μ_s' is the controlled sweep variable,

$$\mu_s = \frac{\mu_s'}{1-g}. \tag{3}$$

A water-dominant refractive index ($n \approx 1.33$) was used as a first-order approximation for boundary behavior in the homogeneous medium model; sensitivity to boundary assumptions is addressed in the Discussion [20,35].

2.2.3. Finite Source and Aperture-Limited Collection (Probe Emulation)

Illumination was modeled as a finite-area LED source [14]. For each wavelength channel and separation $\rho \in \{\rho_c, \rho_f\}$, the LED emission center was positioned at lateral offset ρ relative to the detector/aperture axis on the sample surface, with launch positions sampled uniformly over a finite emitting area consistent with the LED package dimensions [14,18]. Launch directions followed a datasheet-matched, generalized Lambertian divergence.

Photon collection was implemented using the MCmatlab light-collector model co-axial with the aperture at the surface [27,29]. To emulate aperture/tunnel throughput, the collector active diameter was set to 4 mm and photons were additionally filtered by an acceptance cone consistent with the cylindrical tunnel geometry [17,18,29].

2.2.4. LUT Generation, Photon Statistics, and Conditioning

For each phantom condition (10% Intralipid, 20% Intralipid), $\mu_a(\lambda)$ was assigned from the recipe-defined $f_{w,\mathrm{true}}$ and held constant while μ_s' was swept over $\mu_s' \in [0.05, 30]\ \mathrm{cm}^{-1}$ at each wavelength (1450 nm, 1650 nm) and SDS (4.5 mm, 7 mm) [5,10,23,32]. For each (λ, ρ, μ_s') condition, the primary LUT output was the detected photon fraction p_{det} (detected counts normalized by launched photons) within the probe-emulated collector acceptance [27,28]. Unless otherwise stated, $N = 2 \times 10^9$ photons were launched per condition [27,28].

To avoid ill-conditioned LUT regions dominated by photon starvation (especially at the far SDS in highly absorbing regimes), LUT points with insufficient detected counts were flagged and excluded from inversion and/or rerun at higher N such that the ratio curves used for interpolation remained smooth and monotonic over the inversion-relevant range [29]. Experimentally measured spatial ratios were then mapped to the corresponding MC-derived ratio curves to estimate μ_s' consistent with the probe geometry and assigned $\mu_a(\lambda)$; these $\mu_s'(\lambda)$ values are used as inputs to the downstream water-fraction consistency-check model [18,29]. Additional statistical details are provided in Supplementary Materials [27,28].

2.3. Hardware Architecture and Circuit Implementation

The instrument is a four-channel SWIR diffuse-reflectance sensor designed to acquire hydration-sensitive ratio measurements using two wavelengths (1450 nm and 1650 nm) at two source–detector separations (SDS): a close channel ($\rho_c \approx 4.5$ mm) and a far channel ($\rho_f \approx 7$ mm). Illumination is time-multiplexed such that only one LED is active at a time. The amplified photodetector output is conditioned on the main board, digitized by a microcontroller ADC, and streamed to a PC over USB for logging and control. Figure 1 summarizes the system architecture and key circuit blocks. Benchtop validation used an amplified laboratory InGaAs photodetector module (Thorlabs PDAPC8).

2.3.1. Module Partitioning and Optical Channels

The system comprises (i) an optical sensor head with four LEDs arranged as two wavelengths at two SDS around a central collection aperture, (ii) a main board providing power distribution and analog conditioning, and (iii) a control unit (microcontroller + PC interface). Mechanical light-control features (aperture/tunnel and baffle geometry) suppress direct-path crosstalk and preferentially collect multiply scattered photons.

Four measurement channels are defined by wavelength and SDS: 1450 nm (close), 1450 nm (far), 1650 nm (close), and 1650 nm (far). LED drive is provided by a four-channel constant-current sink driver (MPQ3326) controlled via I^{2}C (Figure 1). The implemented channel mapping is CH1 = 1450 nm (close), CH2 = 1650 nm (far), CH3 = 1450 nm (far), and CH4 = 1650 nm (close), corresponding to the physical LED placement. A channel-mapping summary is also provided in the Supplementary Materials (Table S4).

doi:10.20944/preprints202603.0476.v1

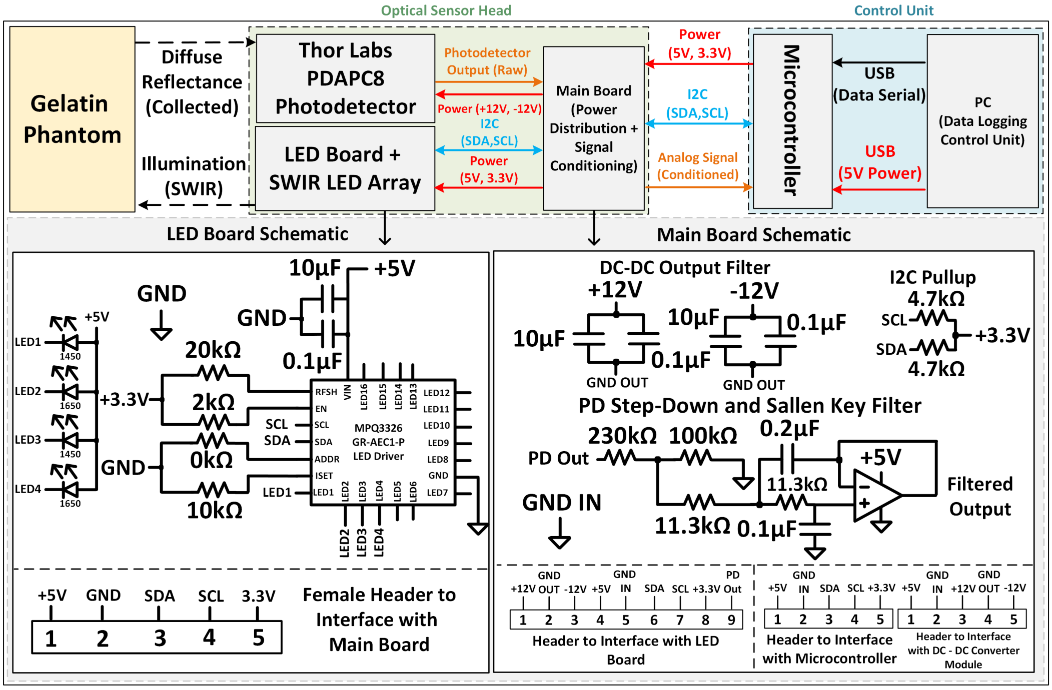

Figure 1. Device block diagram and key schematics. Top: module partitioning and signal/power flow. Bottom: implemented LED-board constant-current drive and main-board power distribution and analog conditioning used to interface the amplified photodetector output to the microcontroller ADC.

2.3.2. Power Distribution and Analog Interface

The main board distributes +5 V and +3.3 V and generates ±12 V rails for the PDAPC8 via a plug-in DC–DC converter (Figure 1). The PDAPC8 analog output is scaled to the ADC input range using a resistive divider and then low-pass filtered prior to digitization. The divider and filter are selected such that the conditioned node remains below ADC saturation while suppressing high-frequency noise for quasi-static intensity measurements under time-multiplexed illumination (full component values and the filter design calculation are provided in Supplementary Materials). All modules share a common ground reference and local decoupling is used to reduce coupling of switched LED currents into the analog sensing path.

2.3.3. Time-multiplexed Measurement Sequence and Acquisition Settings

Measurements are dark-subtracted and normalized to a diffuse reflectance reference (PTFE) to reduce fixed multiplicative differences due to LED radiant power, channel responsivity, and geometry; residual mismatch between reference and sample is treated as a potential contributor to systematic bias. For each gel phantom, one four-channel measurement set (two wavelengths × two SDS) is acquired under consistent probe contact, and a PTFE reference is acquired in close temporal proximity under the same contact geometry. Timing/averaging parameters are summarized in the Supplementary Materials (Table S5).

2.4. Mechanical Implementation and Optical Interface

The optical sensor head is a mechanically registered, light-shielded assembly that enforces fixed source–detector geometry while suppressing direct LED–detector crosstalk. Figure 2 summarizes the head stack-up, sample-facing geometry, and device-level assembly context. A Thorlabs PDAPC8 amplified InGaAs photodetector module is clamped to the LED board, providing repeatable alignment between the detector collection axis and the LED source geometry and minimizing optical head height.

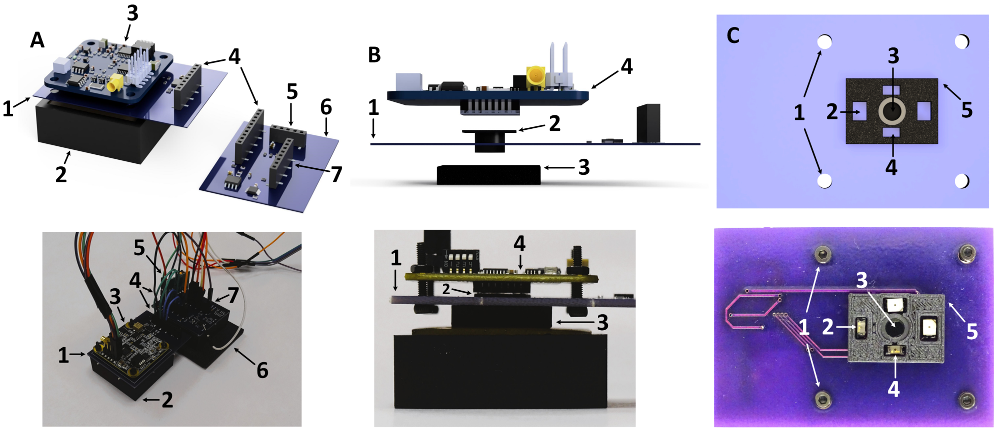

Figure 2. Optical sensor head overview. Top row: CAD renderings showing (A) compact sensor head positioned on the gel phantom, (B) side view of the assembled optical stack, and (C) sample-facing view of the LED emission apertures and central detector tunnel that constrains the photodetector field of view. Bottom row: corresponding photographs. **Callouts:** (A.1) LED board; (A.2) 3D-printed mold holding the gelatin phantom; (A.3) PDAPC8 photodetector module; (A.4) LED-board to main-board interface; (A.5) female header for the DC–DC module; (A.6) main board; (A.7) female header for interfacing with the microcontroller. (B.1) LED board; (B.2) aperture; (B.3) baffle; (B.4) PDAPC8 photodetector module. (C.1) M2.5 screw apertures securing the PDAPC8 to the LED board; (C.2) aperture for the far LEDs; (C.3) photodetector aperture (PDAPC8); (C.4) aperture for the close LEDs; (C.5) rectangular baffle. The PDAPC8 CAD model was obtained from Thorlabs.

2.4.1. Detector Aperture/Tunnel for Field-Of-View Control

A black 3D-printed aperture/tunnel is sandwiched between the PDAPC8 underside and the LED-board center opening to define aperture-limited collection. The flange contains a 4.0 mm diameter circular opening that defines the effective collection aperture, followed by a cylindrical tunnel extending toward the sample. This geometry limits detector field of view and reduces sensitivity to off-axis/stray light, biasing collection toward multiply scattered (diffuse) photons emerging from the sample. A second black 3D-printed baffle block surrounds the source–detector region on the sample side to suppress shortcut optical paths. The baffle includes a central aperture for the detector tunnel and four LED openings positioned at the nominal SDS used here to reduce line-of-sight or near-surface crosstalk that can confound spatially resolved diffuse-reflectance measurements. Together, the clamped detector mounting, aperture/tunnel, and baffle block provide a repeatable optical interface for spatially resolved measurements. Absolute magnitudes can still vary with contact pressure and coupling; accordingly, downstream analysis emphasizes same-wavelength spatial ratios with same-session reference normalization to reduce sensitivity to multiplicative coupling factors.

2.5. Mathematical Inversion and Water-Fraction Consistency-Check Estimation

This section describes the pipeline that converts four electrical measurements (two wavelengths $\times$ two SDS) into (i) wavelength-specific reduced scattering estimates and (ii) a calibration-anchored water-fraction *consistency-check* estimate.

The overall inversion workflow is summarized in Figure 3. A probe-matched MC LUT is used to infer $\mu_s'(\lambda)$ from corrected same-wavelength spatial ratios, and a semi-infinite diffusive spatially resolved spectroscopy (SRS) forward model (dipole formulation) [17,36] is swept over candidate f_w values to compare modeled and measured ratios. In this work, the diffusion/SRS stage is used to assess *directionality and internal consistency* (i.e., whether the recovered $\hat{f}_w$ increases across the phantom series as recipe water fraction increases), rather than to provide a blind, stand-alone estimate of absolute water content for unknown samples. Table 2 summarizes the key notations used to derive the fraction of water in the produced gelatin phantoms.

Preprints.org (www.preprints.org) | NOT PEER-REVIEWED | Posted: 5 March 2026 doi:10.20944/preprints202603.0476.v1

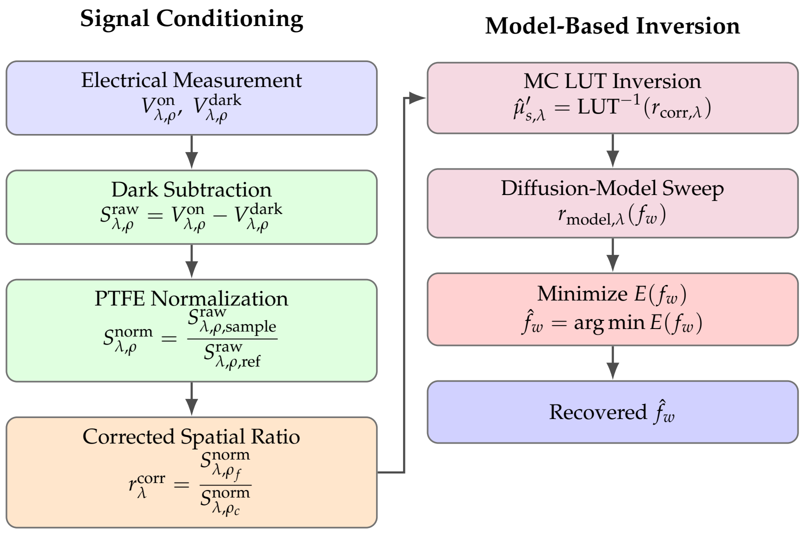

Figure 3. Two-column overview of the inversion pipeline. Left: signal conditioning and formation of corrected spatial ratios. Right: model-based inversion and water-fraction estimation.

Table 2. Key symbols and units used throughout the manuscript.

Symbol	Definition	Units
μ_a	Absorption coefficient	cm^{-1}
$\mu_{a,\lambda}(f_w)$	Absorption coefficient at wavelength λ parameterized by f_w	cm^{-1}
$\mu_{a,\text{water}}(\lambda)$	Absorption coefficient of pure water at wavelength λ	cm^{-1}
μ_s	Scattering coefficient	cm^{-1}
μ'_s	Reduced scattering coefficient ($\mu_s(1-g)$)	cm^{-1}
$\hat{\mu}'_{s,\lambda}$	LUT-inverted reduced scattering coefficient at wavelength λ	cm^{-1}
μ_{eff}	Effective attenuation coefficient	cm^{-1}
g	Anisotropy factor	–
ρ_c	Close source–detector separation	cm
ρ_f	Far source–detector separation	cm
f_w	Candidate bulk water fraction	–
$f_{w,\text{true}}$	Recipe-defined nominal water fraction	–
$\phi_i(f_w)$	Effective fraction of constituent i in absorption mixture model	–
$V^{\text{on}}_{\lambda,\rho}$	Measured photodetector voltage with LED on	V
$V^{\text{dark}}_{\lambda,\rho}$	Measured photodetector voltage with LED off (dark baseline)	V
$S^{\text{raw}}_{\lambda,\rho}$	Dark-subtracted signal	V
$S^{\text{norm}}_{\lambda,\rho}$	Reference (PTFE)-normalized signal	–
$S^{\text{raw}}_{\lambda,\rho,\text{ref}}$	Dark-subtracted signal measured on the PTFE reference	–
$S^{\text{MC}}_{\lambda,\rho}(\mu'_{s,\lambda})$	MC-predicted detected signal at wavelength λ and separation ρ	–
$r^{\text{corr}}_{\lambda}$	Corrected measured far/close spatial ratio	–
r^{MC}_{λ}	Monte Carlo LUT-predicted spatial ratio	–
$r^{\text{model}}_{\lambda}$	Diffusion-model spatial ratio	–
$U_\lambda(\rho; f_w)$	Diffusion-model fluence-rate proxy at separation ρ	a.u.
C_λ	Wavelength-dependent coupling constant	–

2.5.1. Notation, Units, and Measured Channels

Two wavelengths are used, $\lambda \in \{1450, 1650\}$ nm, and two source–detector separations: ρ_c (close) and ρ_f (far):

$$\rho_c = 0.45 \text{ cm}, \qquad \rho_f = 0.70 \text{ cm}. \tag{4}$$

For each measurement cycle, the microcontroller samples the conditioned photodetector voltage for each LED state:

$$V^{\text{on}}_{\lambda,\rho_c}, \qquad V^{\text{on}}_{\lambda,\rho_f}, \qquad \lambda \in \{1450, 1650\} \text{ nm}. \tag{5}$$

An LED-off baseline is recorded immediately before each LED measurement:

$$V_{\lambda,\rho}^{\mathrm{dark}}, \qquad \rho \in \{\rho_c, \rho_f\}. \tag{6}$$

2.5.2. Dark Subtraction and Channel-Wise Normalization

Additive offsets and ambient contributions are removed by dark subtraction:

$$S_{\lambda,\rho}^{\mathrm{raw}} = V_{\lambda,\rho}^{\mathrm{on}} - V_{\lambda,\rho}^{\mathrm{dark}}, \qquad \rho \in \{\rho_c, \rho_f\}. \tag{7}$$

Because close and far channels use distinct emitters, same-session reference normalization (PTFE) is used to suppress channel-to-channel scale factors:

$$S_{\lambda,\rho}^{\mathrm{norm}} = \frac{S_{\lambda,\rho,\mathrm{sample}}^{\mathrm{raw}}}{S_{\lambda,\rho,\mathrm{ref}}^{\mathrm{raw}}}. \tag{8}$$

2.5.3. Corrected Measured Spatial Ratios (PTFE Applied Once)

A corrected same-wavelength spatial ratio is then formed:

$$r_\lambda^{\mathrm{corr}} = \frac{S_{\lambda,\rho_f}^{\mathrm{norm}}}{S_{\lambda,\rho_c}^{\mathrm{norm}}} = \frac{S_{\lambda,\rho_f,\mathrm{sample}}^{\mathrm{raw}}}{S_{\lambda,\rho_c,\mathrm{sample}}^{\mathrm{raw}}} \cdot \frac{S_{\lambda,\rho_c,\mathrm{ref}}^{\mathrm{raw}}}{S_{\lambda,\rho_f,\mathrm{ref}}^{\mathrm{raw}}}. \tag{9}$$

In what follows, transport-model ratios (MC LUT and diffusion) are matched directly to $r_\lambda^{\mathrm{corr}}$; absolute signal magnitudes are not interpreted in this study.

2.5.4. MC LUT Inversion for Reduced Scattering (Ratio Matching in the Corrected Domain)

For each wavelength, the MC LUT provides the probe-matched ratio

$$r_\lambda^{\mathrm{MC}}(\mu'_{s,\lambda}) = \frac{S_{\lambda,\rho_f}^{\mathrm{MC}}(\mu'_{s,\lambda})}{S_{\lambda,\rho_c}^{\mathrm{MC}}(\mu'_{s,\lambda})}, \tag{10}$$

where r_λ^{MC} is the LUT-predicted ratio and SMC denotes the MC-predicted signal.

Over the inversion-relevant range, $r_\lambda^{\mathrm{MC}}(\mu'_s)$ is monotonic, enabling one-dimensional inversion. $\hat{\mu}'_{s,\lambda}$ is computed by interpolation between neighboring LUT points. If two LUT entries (μ'_1, r_1) and (μ'_2, r_2) bracket the measurement, log-domain interpolation in the ratio is used:

$$\hat{\mu}'_{s,\lambda} = \mu'_1 + (\mu'_2 - \mu'_1)\,\frac{\ln(r_\lambda^{\mathrm{corr}}) - \ln(r_1)}{\ln(r_2) - \ln(r_1)}. \tag{11}$$

Where μ'_1 and μ'_2 are the two bracketing LUT scattering values (units cm^{-1}), r_1 and r_2 are the corresponding LUT ratios (unitless), and $\ln(\cdot)$ denotes the natural logarithm.

Measurements yielding non-positive normalized signals are flagged as low-SNR and excluded from inversion to avoid undefined logarithms. Where SNR denotes signal-to-noise ratio.

2.5.5. Absorption Model Parameterized by Water Fraction (Assigned, Not Estimated, in This Study)

After scattering is estimated from the LUT, absorption is parameterized by a candidate bulk water fraction $f_w \in [0, 1]$. A general mixture model can be written as

$$\mu_{a,\lambda}(f_w) = \sum_i \phi_i(f_w)\,\mu_{a,i}(\lambda), \tag{12}$$

and is approximated here as water dominated over the two-wavelength set:

$$\mu_{a,\lambda}(f_w) \approx f_w\,\mu_{a,\mathrm{water}}(\lambda). \tag{13}$$

Finite LED spectral bandwidth (especially near 1450 nm) and any non-water absorption/effective-medium effects that vary with Intralipid loading are treated as limitations; in this validation, $\mu_{a,\lambda}$ used for LUT generation/inversion is assigned from nominal $f_{w,\text{true}}$, so any recovered $\hat{f}_w$ from the forward-model sweep is interpreted as a consistency check rather than blind absorption estimation.

2.5.6. Diffusion/SRS Forward Model

To relate candidate water fraction to expected spatial falloff, we use a semi-infinite diffusion-based dipole model as a parametric signal proxy [17,36]. Using the standard dipole construction with extrapolated boundary conditions [17,36], the predicted intensity (up to an unknown multiplicative coupling constant C_λ) is

$$U_\lambda(\rho; f_w) = \frac{C_\lambda}{4\pi D_\lambda(f_w)} \left(\frac{e^{-\mu_{\text{eff},\lambda}(f_w)\, r_{1,\lambda}(\rho;f_w)}}{r_{1,\lambda}(\rho; f_w)} - \frac{e^{-\mu_{\text{eff},\lambda}(f_w)\, r_{2,\lambda}(\rho;f_w)}}{r_{2,\lambda}(\rho; f_w)} \right), \tag{14}$$

where $r_{1,\lambda}$ and $r_{2,\lambda}$ are the source and image-source distances defined by the dipole geometry (computed as in [17,36] using a first-order refractive index $n = 1.33$; full boundary-parameter expressions are provided in Supplementary Materials).

U_λ is the diffusion-model fluence-rate proxy and C_λ is a wavelength-dependent coupling constant. The modeled same-wavelength spatial ratio is then

$$r_\lambda^{\text{model}}(f_w) = \frac{U_\lambda(\rho_f; f_w)}{U_\lambda(\rho_c; f_w)}, \tag{15}$$

where $r_\lambda^{\text{model}}(f_w)$ is the diffusion-model spatial-ratio proxy (unitless) at wavelength λ as a function of candidate water fraction f_w.

In Eq. (14), the unknown coupling factor C_λ and the prefactor $(4\pi D_\lambda)^{-1}$ cancel, so the ratio depends only on separation and the optical-property terms derived from $\mu_{a,\lambda}(f_w)$ and $\hat{\mu}'_{s,\lambda}$. Because PTFE normalization is already applied once in r_λ^{corr} (Eq. (9)), no reference term is included inside the transport-model ratio.

2.5.7. Error Function and Water-Fraction Minimization (Consistency-Check Estimate)

Candidate f_w values are evaluated by comparing modeled and corrected measured spatial ratios using a log-domain squared error:

$$E(f_w) = \sum_{k=1}^{K} \left[\ln\!\left(r_k^{\text{corr}}\right) - \ln\!\left(r_k^{\text{model}}(f_w)\right) \right]^2, \tag{16}$$

where $E(f_w)$ is the scalar (unitless) error assigned to candidate f_w, k indexes the set of ratio constraints included in the consistency-check objective (e.g., wavelengths and/or measurement channels), and K is the number of terms used.

A bounded sweep is performed over a physically plausible interval $\mathcal{F} \subset [0, 1]$, and the final estimate is

$$\hat{f}_w = \arg \min_{f_w \in \mathcal{F}} E(f_w). \tag{17}$$

where $\mathcal{F}$ is the chosen feasible set of candidate water fractions. In this study, $\hat{f}_w$ is interpreted as a calibration-anchored consistency-check estimate under the absorption assignment and modeling assumptions used; across the phantom series, the primary expectation is that $\hat{f}_w$ increases monotonically with recipe-defined $f_{w,\text{true}}$ under the stated conditioning. Extension to unknown samples would require coupling the absorption-conditional LUT step to the f_w sweep (e.g., a 2D LUT over (μ_a, μ'_s) or an iterative scheme), which is outside the validated scope here.

doi:10.20944/preprints202603.0476.v1

2.5.8. Interpretation Considerations and Failure Modes

Practical failure modes include: (i) phantom non-homogeneity (stratification), which violates the single (μ_a, μ_s') per wavelength assumption; and (ii) mismatch between the recipe-defined water-fraction reference and the absorption proxy in Eq. (13) (e.g., differing treatment of Intralipid solvent water or mass-fraction-as-volume-fraction approximations); (iii) finally, because LUT inversion is conditional on assigned absorption, any deviation between assigned and effective $\mu_{a,\lambda}$ propagates into $\hat{\mu}'_{s,\lambda}$ and can bias the subsequent consistency-check estimate.

3. Results

3.1. Monte Carlo LUT Characterization and Scattering Observables

Geometry-matched Monte Carlo (MC) simulations were used to generate lookup tables (LUTs) that relate reduced scattering coefficient μ_s' to expected diffuse-reflectance observables for the four optical channels (1450 nm and 1650 nm at 4.5 mm and 7 mm source–detector separations). For each phantom water-fraction condition, MC simulations were run using absorption coefficients computed from the formulation-derived bulk water fraction $f_{w,\mathrm{true}}$ (water-dominant absorption parameterization) while sweeping μ_s' over the range of interest. The coupling required for unknown samples is described in Section 2.5. Representative log-scale magnitude LUT sweeps are provided in the Supplementary Materials (Fig. S2) and are used primarily to verify channel ordering and dynamic-range behavior. Full LUT tables are provided in the Supplementary Materials (Tables S7–S10). For visualization, the 1450 nm and 1650 nm far/close LUTs are also shown as interpolated 3D surfaces over added-water fraction and μ_s' in Figure 4.

To isolate a scattering-sensitive observable that is robust to unknown scale factors (LED radiant power, coupling, detector responsivity, and gain), same-wavelength far/close ratios were computed from the LUTs. Figure 4 shows that the far/close ratio at each wavelength is monotonic with μ_s', enabling μ_s' inversion via interpolation. The relatively small separation between ratio curves across different f_w is expected because same-wavelength spatial ratios largely suppress common multiplicative scaling; in this construction, curve-to-curve shifts reflect absorption-dependent transport differences (through the $f_w \to \mu_a$ assignment) rather than arbitrary LED scaling.

The 1450 nm ratio exhibits a more compressed dynamic range than 1650 nm, consistent with stronger water absorption at 1450 nm suppressing longer photon paths and reducing far/close contrast. In practice, scattering recovery is performed within the μ_s' regimes relevant to the experimental phantoms. For clarity, Figure 4 includes zoomed views around the recovered μ_s' ranges for the 10% and 20% Intralipid datasets, with inversion markers overlaid.

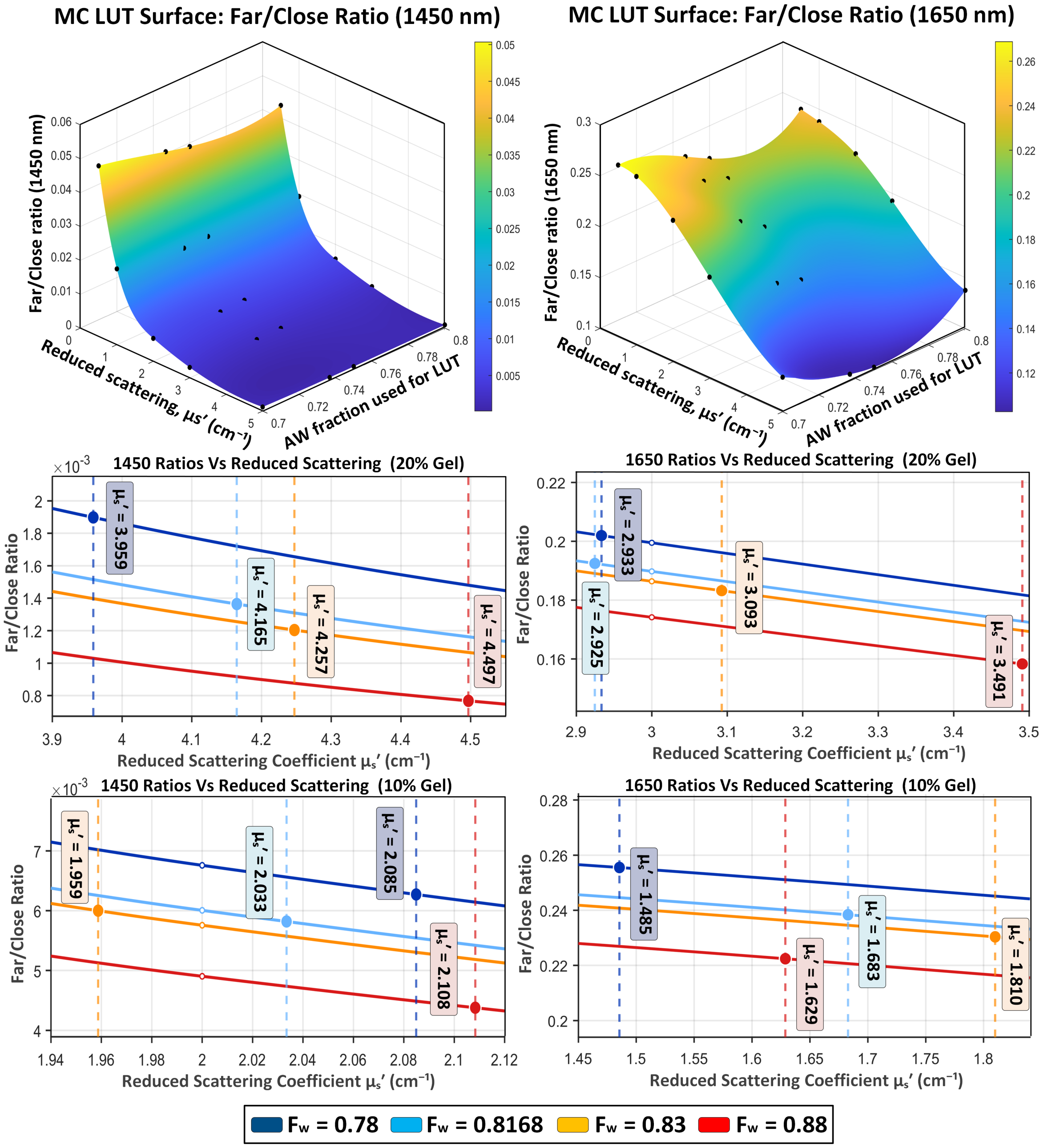

Figure 4. Monte Carlo (MC) lookup-table (LUT) visualization of same-wavelength far/close spatial ratios for gelatin–Intralipid phantoms at 1450 nm (left column) and 1650 nm (right column). Top row: interpolated 3D LUT surfaces of the MC-predicted far/close ratio $r_{\mathrm{MC},\lambda} = S_{\lambda,\rho_f}/S_{\lambda,\rho_c}$ shown versus reduced scattering coefficient μ_s' and the added-water (AW) condition used to assign $\mu_a(\lambda)$ during LUT generation; black points indicate the discrete simulated LUT entries. Middle row: zoomed ratio-curve views versus μ_s' for the 20% Intralipid dataset. Bottom row: zoomed ratio-curve views versus μ_s' for the 10% Intralipid dataset. In each zoomed panel, vertical dashed lines indicate the LUT-inverted $\hat{\mu}_s'$ values for each phantom and filled markers denote the intersection of each inversion line with its corresponding ratio curve. For readability, the 1450 nm ratio panels are displayed with a $\times 10^3$ scale factor. Curves/markers are grouped by the formulation-derived reference water fraction $f_{w,\mathrm{true}}$ (color-coded).

3.2. Water-Fraction Consistency-Check Agreement Analysis

Using the corrected measured spatial ratios and the absorption-conditional MC-derived scattering estimates (via LUT interpolation), a diffusion/SRS forward-model sweep was performed as a calibration-anchored consistency check on eight Intralipid-containing gelatin phantoms (four phantoms at 10% Intralipid stock loading and four phantoms at 20% Intralipid stock loading). In this controlled phantom-validation analysis, $\mu_a(\lambda)$ was parameterized using the recipe-defined nominal $f_{w,\mathrm{true}}$ (via the water-dominant model described in Section 2.5) to evaluate whether the pipeline preserves the nominal ordering and values of $f_{w,\mathrm{true}}$ under absorption-consistent conditions. Each value reported corresponds to a single averaged measurement per phantom under a fixed acquisition configuration.

Across the eight Intralipid-containing phantoms, the recovered f_w values preserved the expected ordering with $f_{w,\mathrm{true}}$ and yielded a mean absolute percent error of 1.55% with a maximum absolute percent error of 3.33% (Table 3), conditional on the recipe-defined absorption parameterization. Errors were larger in the 10% Intralipid dataset (mean absolute percent error 2.36%) than in the 20% Intralipid dataset (0.74%). The differences were predominantly negative (SRS underestimation), suggesting that the dominant error component in this dataset is systematic rather than purely random scatter. In addition, the LUT stage produced wavelength-specific scattering estimates in the expected Intralipid regime (Table 3), supporting that the spatial-ratio inversion was operating within a well-conditioned region of the ratio curves.

Although the primary hydration sensitivity is expected near 1450 nm, the 1650 nm band provides a complementary constraint because it lies in a lower-absorption water band and can be less susceptible to modeling mismatch near the steep 1450 nm absorption peak (e.g., finite LED bandwidth and effective μ_a). In the two-wavelength formulation (Eq. 16), this secondary band helps regularize the f_w sweep by reducing reliance on a single wavelength term, and it provides additional leverage to distinguish absorption-driven and scattering-driven changes in the measured spatial ratios.

Agreement is visualized using an identity plot (Figure 5, middle), which compares the recovered water fraction $\hat{f}_w$ to the formulation-derived reference $f_{w,\mathrm{true}}$ with the $y = x$ line indicating perfect agreement. The identity plot highlights the overall clustering near the diagonal as well as a consistent negative offset across most phantoms. For this dataset ($n = 8$), the overall bias (SRS−reference) was -0.0122 (absolute water-fraction units), with MAE $= 0.0125$ and RMSE $= 0.0156$.

To illustrate sensitivity to LUT selection (i.e., absorption-conditionality of the ratio-to-μ_s' mapping), Figure 5 also includes a "75% nominal" comparison (bottom), where a single LUT condition is applied across gels rather than using recipe-conditioned LUTs. This fixed-LUT case visibly deviates from the theoretical trend, motivating coupled or expanded LUT strategies (e.g., 2D LUTs over (μ_a, μ_s') or iterative LUT selection during the f_w sweep) for truly unknown samples in the future.

Table 3. Comparison of formulation-derived reference water fraction and SRS-recovered water fraction for gelatin–Intralipid phantoms. Gel IDs report the *added-water fraction* used during formulation (excluding solvent water contained in Intralipid stock). For the 20% group, added-water fractions are adjusted so that the reference $f_{w,\mathrm{true}}$ matches the corresponding 10% targets (Table 1). Absolute percent error is computed as $\left|\hat{f}_w - f_{w,\mathrm{true}}\right| / f_{w,\mathrm{true}} \times 100$.

Gel ID	**IL (wt%)**	$\hat{\mu}'_{s,1450}$	$\hat{\mu}'_{s,1650}$	$f_{w,\mathrm{true}}$	$\hat{f}_w$	**Abs. Error (%)**
10% Intralipid						
AW70	10	2.085	1.485	0.780	0.754	3.333
AW73.68	10	2.033	1.683	0.817	0.800	2.081
AW75	10	1.959	1.810	0.830	0.824	0.723
AW80	10	2.108	1.629	0.880	0.851	3.295
20% Intralipid						
AW62	20	3.959	2.933	0.780	0.771	1.154
AW65.68	20	4.165	2.925	0.817	0.811	0.734
AW67	20	4.247	3.093	0.830	0.823	0.843
AW72	20	4.497	3.491	0.880	0.882	0.227

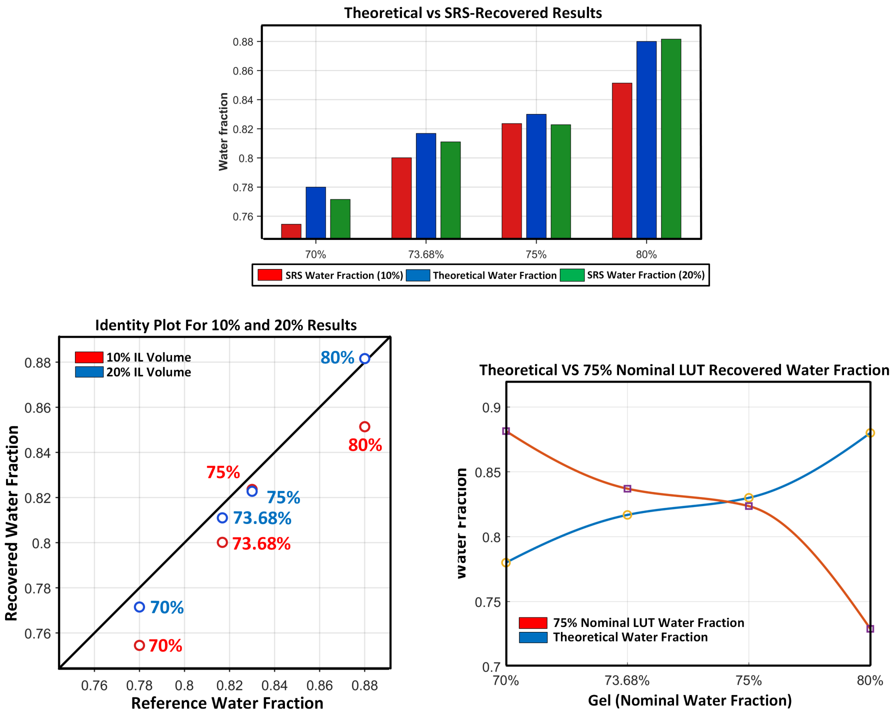

Figure 5. Combined results figure summarizing water-fraction recovery and a fixed-LUT sensitivity check. Top: recovered $\hat{f}_w$ (SRS) and reference $f_{w,\mathrm{true}}$ grouped by phantom condition (10% and 20% Intralipid stock loading). Bottom Left: identity plot of $\hat{f}_w$ versus $f_{w,\mathrm{true}}$; the diagonal line indicates $y = x$ (perfect agreement). Bottom Right: "75% nominal" LUT comparison showing theoretical water fraction versus the recovered trend when using a single nominal LUT condition across gels rather than recipe-conditioned LUTs.

4. Discussion

4.1. Principal Findings

This study demonstrates a probe-geometry-matched, two-step analysis pipeline for SWIR diffuse reflectance using two wavelengths (1450 nm and 1650 nm) and two source–detector separations (4.5 mm and 7 mm). Probe-specific Monte Carlo (MC) lookup tables (LUTs) map same-wavelength spatial ratios to reduced scattering μ_s', and the resulting $\mu_s'(\lambda)$ values are used in a semi-infinite diffusive SRS forward model to perform a feasibility study to detect water-fraction in homogeneous media. In this phantom-validation configuration, $\mu_a(\lambda)$ is assigned from the recipe-defined (nominal) phantom water fraction (with stated uncertainty) rather than estimated from reflectance; therefore, recovered $\hat{f}_w$ values reflect conditional recovery under controlled assumptions rather than blind inference for unknown tissue samples. This approach establishes the intrinsic hydration sensitivity, stability, and internal consistency of the measurement geometry and inversion framework, creating a validated baseline against which future coupled absorption–scattering implementations can be rigorously evaluated.

Across eight Intralipid-containing gelatin phantoms spanning formulation-derived theoretical $f_w \approx 0.78$–0.88, recovered water fractions preserved the expected ordering and agreed with theoretical values with a mean absolute percent error of 1.55% and a maximum absolute percent error of 3.33% (Table 3). The identity-plot agreement showed a consistent negative bias (systematic underestimation) rather than large random scatter (Figure 5, middle), indicating stable behavior under fixed acquisition conditions but motivating refinement to reduce offset. The same combined results figure also includes a "75% nominal" fixed-LUT comparison (Figure 5, bottom), which illustrates the sensitivity of recovered trends to LUT selection when absorption is not matched to each phantom condition.

4.2. Physical Interpretation of Scattering Observables and Spatial Ratios

The MC LUTs support two practical conclusions for the measurement design. First, channel magnitudes span a wide dynamic range across μ_s' and across wavelengths/SDS, so log-scale visualization is useful (see Supplementary Fig. S2); the inversion itself relies on ratio observables and compares ratios in the log domain to emphasize multiplicative mismatch and reduce sensitivity to residual scale factors. Second, same-wavelength far/close ratios provide a compact observable for scattering recovery because many session-specific multiplicative factors are reduced by reference normalization and ratio formation. The ratio remains jointly dependent on scattering and absorption through distance-dependent attenuation, but is monotonic in μ_s' over the phantom regimes studied, enabling interpolation-based inversion.

Figure 4 provides an additional geometric and conditioning perspective by visualizing the far/close LUTs as interpolated 3D surfaces over the LUT parameter axes (added-water condition used to assign $\mu_a(\lambda)$ and μ_s'). The smooth surface structure and absence of folds in the operating region indicate that the ratio-to-μ_s' mapping is well behaved for these phantom regimes, and the overlaid discrete simulation points verify that the surface interpolation is not introducing obvious artifacts. The corresponding zoomed 2D panels (Figure 4, middle and bottom rows) make explicit where the experimental inversions lie on these surfaces/curves and show that the inverted $\hat{\mu}_s'$ values occur within the monotonic, well-conditioned portion of each ratio curve for both 10% and 20% Intralipid datasets.

Differences between 1450 nm and 1650 nm behavior are physically consistent. Stronger water absorption at 1450 nm suppresses longer photon paths, compressing far/close contrast relative to 1650 nm. At 1650 nm, reduced absorption permits a larger contribution of longer paths to the far separation, yielding larger ratio dynamic range and potentially improved sensitivity to μ_s' in the operating regime. Moreover, including both wavelengths provides complementary constraints for downstream consistency-check estimation: 1450 nm offers strong hydration sensitivity near the dominant water band, while 1650 nm lies in a lower-absorption water band and can be less susceptible to modeling mismatch near the steep 1450 nm peak (e.g., finite LED bandwidth and effective μ_a). The close separation provides higher SNR superficial sampling, while the far separation increases sensitivity to optical-property changes that affect spatial falloff at the cost of lower magnitude.

4.3. Limitations and Sources of Systematic Bias

Few factors condition the interpretation of the agreement metrics. First, the dataset is modest ($n = 8$), with one averaged measurement per phantom; thus, reported bias and absolute error values are descriptive of this configuration rather than population-level performance bounds.

Second, the inversion framework is hybrid: probe-geometry-matched Monte Carlo (MC) lookup tables (LUTs) recover μ_s', while a semi-infinite diffusion model provides the water-fraction sweep. Diffusion theory is approximate at millimeter-scale source–detector separations in strongly absorbing SWIR bands, and deviations from semi-infinite assumptions (finite phantom thickness, boundary effects, contact variability, and aperture constraints) can introduce systematic offsets.

Third, LUT-based scattering recovery is absorption-conditional. In this validation, $\mu_a(\lambda)$ was assigned from the recipe-defined $f_{w,\text{true}}$ to evaluate internal consistency under controlled conditions. For unknown samples, this conditionality must be removed via coupled strategies, such as a 2D LUT over (μ_a, μ_s') or iterative absorption–scattering updates during the f_w sweep.

The fixed-LUT comparison shown in Fig. 5 directly illustrates this dependence: applying a single nominal absorption condition across gels disrupts ordering and magnitude agreement, confirming that far/close spatial ratios depend jointly on μ_a and μ_s'.

Despite these constraints, the results demonstrate that the compact probe architecture preserves monotonic hydration trends and achieves $<$ 3.33% maximum absolute error under absorption-consistent conditions, establishing geometric and transport-model fidelity necessary for extension to blind inversion frameworks.

4.4. Implications and Next Steps

These phantom-validation results demonstrate that a compact SWIR reflectance probe produces repeatable, monotonic spatial-ratio signatures with respect to recipe-defined water fraction in gelatin–Intralipid media under absorption-parameterized conditions. The study therefore establishes hydration-sensitive signal behavior and inversion self-consistency in a controlled optical setting, rather than serving as a blind estimator of tissue water fraction. The findings motivate targeted refinements to improve SNR, tighten control of effective source–detector separation, and strengthen correspondence between hardware and Monte Carlo (MC) models.

For translation to unknown samples, two modeling upgrades are indicated: (i) generate LUTs over a 2D grid of $(\mu_a, \mu_s^{'})$ (or equivalently ($(f_w, \mu_s^{'})$) with an explicit absorption model) to enable coupled scattering inversion during the sweep, and/or (ii) implement an iterative scheme in which a candidate f_w defines $\mu_a(\lambda)$) selects the appropriate LUT slice, updates $\mu_s^{'}(\lambda)$), and repeats to convergence. Either strategy removes reliance on recipe-conditioned absorption and enables principled blind recovery with uncertainty quantification.

On the hardware side, closer alignment between the MC source model and physical emission geometry is required. Because discrete LEDs launch from finite standoff with angular sensitivity, an aperture-defined effective source is recommended: combine same-wavelength LEDs into a short mixing element (e.g., light pipe or integrating cavity) terminating at a fixed exit aperture with a precisely defined offset. This approach increases photon budget and SNR while providing a well-defined MC boundary condition. Similarly, adding a defined collection optic (e.g., light guide or concentrator) can stabilize acceptance geometry and improve repeatability; such changes can be incorporated into future LUT generation.

Finally, mismatched package dimensions between the 1450 nm and 1650 nm LEDs introduced small but systematic differences in effective source position and launch conditions that are difficult to fully capture in simplified MC models. A clear next step is to use wavelength-matched LEDs in identical, smaller-footprint, higher-radiance packages so both channels share a common mechanical datum, improving geometric consistency and optical power simultaneously.

Supplementary Materials: The following supporting information can be downloaded at the website of this paper posted on Preprints.org.

Author Contributions: Conceptualization, G.F. and A.T.Z.; methodology, G.F. and A.T.Z.; hardware and software, G.F. and D.V.; experiments and data analysis, G.F.; supervision, A.T.Z.; writing—original draft, G.F.; writing—review and editing, all authors.

Funding: This research received no external funding.

Acknowledgments: The authors acknowledge Texas A&M University facilities and support for prototyping and testing.

Conflicts of Interest: The authors declare no conflict of interest.

References

1. Wiig, H. Pathophysiology of tissue fluid accumulation in inflammation. *The Journal of physiology* **2011**, *589*, 2945–2953.
2. Smith, A.G.; Perez, R.; Thomas, A.; Stewart, S.; Samiei, A.; Bangalore, A.; Gomer, H.; Darr, M.B.; Schweitzer, R.C.; Vasudevan, S.; et al. Objective determination of peripheral edema in heart failure patients using short-wave infrared molecular chemical imaging. *Journal of Biomedical Optics* **2021**, *26*, 105002–105002.
3. Brodovicz, K.G.; McNaughton, K.; Uemura, N.; Meininger, G.; Girman, C.J.; Yale, S.H. Reliability and feasibility of methods to quantitatively assess peripheral edema. *Clinical medicine & research* **2009**, *7*, 21–31.
4. Roblyer, D.; Pilvar, A.; Pham, T.; Spink, S.; Hayakawa, C.K.; Venugopalan, V.; Pierce, M.C. Review of shortwave infrared imaging and spectroscopy in tissue. *Biomedical Optics Express* **2025**, *16*, 5028–5062.
5. Jacques, S.L. Optical properties of biological tissues: a review. *Physics in medicine and biology* **2013**, *58*, R37–R61.

6. Mamouei, M.; Chatterjee, S.; Razban, M.; Qassem, M.; Kyriacou, P.A. Design and analysis of a continuous and non-invasive multi-wavelength optical sensor for measurement of dermal water content. *Sensors* **2021**, *21*, 2162.
7. Hale, G.M.; Querry, M.R. Optical constants of water in the 200-nm to 200-μ m wavelength region. *Applied optics* **1973**, *12*, 555–563.
8. Wilson, R.H.; Nadeau, K.P.; Jaworski, F.B.; Tromberg, B.J.; Durkin, A.J. Review of short-wave infrared spectroscopy and imaging methods for biological tissue characterization. *Journal of biomedical optics* **2015**, *20*, 030901–030901.
9. Nachabe, R.; Hendriks, B.H.; Desjardins, A.E.; van der Voort, M.; van der Mark, M.B.; Sterenborg Henricus, J. Estimation of lipid and water concentrations in scattering media with diffuse optical spectroscopy from 900 to 1600 nm. *Journal of biomedical optics* **2010**, *15*, 037015–037015.
10. Troy, T.L.; Thennadil, S.N. Optical properties of human skin in the near infrared wavelength range of 1000 to 2200 nm. *Journal of biomedical optics* **2001**, *6*, 167–176.
11. Gidado, I.M.; Qassem, M.; Triantis, I.F.; Kyriacou, P.A. Review of advances in the measurement of skin hydration based on sensing of optical and electrical tissue properties. *Sensors* **2022**, *22*, 7151.
12. Zhao, Y.; Pilvar, A.; Tank, A.; Peterson, H.; Jiang, J.; Aster, J.C.; Dumas, J.P.; Pierce, M.C.; Roblyer, D. Shortwave-infrared meso-patterned imaging enables label-free mapping of tissue water and lipid content. *Nature communications* **2020**, *11*, 5355.
13. Spink, S.S. Next generation near infrared (NIR) and shortwave infrared (SWIR) wearables for breast cancer imaging. PhD thesis, Boston University, 2023.
14. Lee, J.Y.; Ahn, S.; Nam, S.H. Performance estimation of optical skin probe in short wavelength infrared spectroscopy based on Monte-Carlo simulation. *Scientific reports* **2022**, *12*, 20134.
15. Visser, C.; Kieser, E.; Dellimore, K.; van den Heever, D.; Smith, J. Investigation of the feasibility of non-invasive optical sensors for the quantitative assessment of dehydration. *Medical Engineering & Physics* **2017**, *48*, 181–187.
16. Volkova, E.; Perchik, A.; Pavlov, K.; Nikolaev, E.; Ayuev, A.; Park, J.; Chang, N.; Lee, W.; Kim, J.Y.; Doronin, A.; et al. Multispectral sensor fusion in SmartWatch for in situ continuous monitoring of human skin hydration and body sweat loss. *Scientific Reports* **2023**, *13*, 13371.
17. Farrell, T.J.; Patterson, M.S.; Wilson, B. A diffusion theory model of spatially resolved, steady-state diffuse reflectance for the noninvasive determination of tissue optical properties in vivo. *Medical physics* **1992**, *19*, 879–888.
18. Kienle, A.; Lilge, L.; Patterson, M.S.; Hibst, R.; Steiner, R.; Wilson, B.C. Spatially resolved absolute diffuse reflectance measurements for noninvasive determination of the optical scattering and absorption coefficients of biological tissue. *Applied optics* **1996**, *35*, 2304–2314.
19. Naglič, P.; Pernuš, F.; Likar, B.; Bürmen, M. Estimation of optical properties by spatially resolved reflectance spectroscopy in the subdiffusive regime. *Journal of Biomedical Optics* **2016**, *21*, 095003–095003.
20. Kienle, A.; Patterson, M.S. Improved solutions of the steady-state and the time-resolved diffusion equations for reflectance from a semi-infinite turbid medium. *Journal of the Optical Society of America A* **1997**, *14*, 246–254.
21. Bevilacqua, F.; Depeursinge, C. Monte Carlo study of diffuse reflectance at source–detector separations close to one transport mean free path. *Journal of the Optical Society of America A* **1999**, *16*, 2935–2945.
22. Pogue, B.W.; Patterson, M.S. Review of tissue simulating phantoms for optical spectroscopy, imaging and dosimetry. *Journal of biomedical optics* **2006**, *11*, 041102–041102.
23. Flock, S.T.; Jacques, S.L.; Wilson, B.C.; Star, W.M.; van Gemert, M.J. Optical properties of Intralipid: a phantom medium for light propagation studies. *Lasers in surgery and medicine* **1992**, *12*, 510–519.
24. Jonasson, H.; Anderson, C.D.; Saager, R.B. Water and hemoglobin modulated gelatin-based phantoms to spectrally mimic inflamed tissue in the validation of biomedical techniques and the modeling of microdialysis data. *Journal of Biomedical Optics* **2022**, *27*, 074712–074712.
25. Lai, P.; Xu, X.; Wang, L.V. Dependence of optical scattering from Intralipid in gelatin-gel based tissue-mimicking phantoms on mixing temperature and time. *Journal of biomedical optics* **2014**, *19*, 035002–035002.
26. Di Ninni, P.; Martelli, F.; Zaccanti, G. Effect of dependent scattering on the optical properties of Intralipid tissue phantoms. *Biomedical optics express* **2011**, *2*, 2265–2278.
27. Marti, D.; Aasbjerg, R.N.; Andersen, P.E.; Hansen, A.K. MCmatlab: an open-source, user-friendly, MATLAB-integrated three-dimensional Monte Carlo light transport solver with heat diffusion and tissue damage. *Journal of biomedical optics* **2018**, *23*, 121622–121622.

28. Wang, L.; Jacques, S.L.; Zheng, L. MCML—Monte Carlo modeling of light transport in multi-layered tissues. *Computer methods and programs in biomedicine* **1995**, *47*, 131–146.
29. Hennessy, R.; Lim, S.L.; Markey, M.K.; Tunnell, J.W. Monte Carlo lookup table-based inverse model for extracting optical properties from tissue-simulating phantoms using diffuse reflectance spectroscopy. *Journal of biomedical optics* **2013**, *18*, 037003–037003.
30. Martelli, F.; Ninni, P.D.; Zaccanti, G.; Contini, D.; Spinelli, L.; Torricelli, A.; Cubeddu, R.; Wabnitz, H.; Mazurenka, M.; Macdonald, R.; et al. Phantoms for diffuse optical imaging based on totally absorbing objects, part 2: experimental implementation. *Journal of biomedical optics* **2014**, *19*, 076011–076011.
31. Goldfain, A.M.; Lemaillet, P.; Allen, D.W.; Briggman, K.A.; Hwang, J. Polydimethylsiloxane tissue-mimicking phantoms with tunable optical properties. *Journal of biomedical optics* **2022**, *27*, 074706–074706.
32. Michels, R.; Foschum, F.; Kienle, A. Optical properties of fat emulsions. *Optics express* **2008**, *16*, 5907–5925.
33. Spinelli, L.; Botwicz, M.; Zolek, N.; et al. Determination of reference values for optical properties of liquid phantoms based on Intralipid and India ink. *Biomedical Optics Express* **2014**, *5*, 2037–2053. https://doi.org/10.1364/BOE.5.002037.
34. Cook, J.R.; Bouchard, R.R.; Emelianov, S.Y. Tissue-mimicking phantoms for photoacoustic and ultrasonic imaging. *Biomedical Optics Express* **2011**, *2*, 3193–3206. https://doi.org/10.1364/BOE.2.003193.
35. Haskell, R.C.; Svaasand, L.O.; Tsay, T.T.; Feng, T.C.; McAdams, M.S.; Tromberg, B.J. Boundary conditions for the diffusion equation in radiative transfer. *Journal of the Optical Society of America A* **1994**, *11*, 2727–2741.
36. Mao, J.J.; Xu, R.; Lash, B.; Wright, L. Quantitative evaluation of ViOptix's tissue oximeter in an ex-vivo animal model. In Proceedings of the Design and Quality for Biomedical Technologies. SPIE, 2008, Vol. 6849, pp. 71–82.